The Hunt for Recoiled Black Holes in the Milky Way's Halo

by

Allyssa Riley

A senior thesis submitted in partial fulfillment of the requirements for graduation with

DEPARTMENTAL HONORS

from the department of

ASTROPHYSICAL AND PLANETARY SCIENCES

at the University of Colorado

Defended on 19 October 2015

Committee Members:

Advisor: Dr. Jeremy Darling, Dept. of Astrophysical and Planetary Science

Dr. Erica Ellingson, Dept. of Astrophysical and Planetary Science

Dr. Adam Norris, Dept. of Applied Mathematics

Dr. Jason Glenn, Dept. of Astrophysical and Planetary Science

Dr. Ryan O'Leary, JILA

Abstract

Since black holes inhabit galactic centers, when galaxies merge, so must their central black holes. If the two coalescing black holes emit anisotropic gravitational waves, one of the black holes can be ejected from the galactic center, bringing a core of stars with it. Based on the merger history of the Milky Way, it is estimated there are ∼300 recoiled black holes in the halo. We present a preliminary spectroscopic search, using the search criteria and list of candidates in O'Leary & Loeb (2012). Although we did not find candidate recoiled black holes, we further optimized the search criteria, using Sloan Digital Sky Survey (SDSS) and Wide-field Infrared Survey Explorer (WISE) magnitudes and colors. More specifically, the SDSS colors $(g - r)$, and $(r - i)$ allow us to constrain the search criteria. Our results contribute to making the search for recoiled black holes more efficient, reducing the amount of false positives that are observed. In the event that a recoiled black hole is found, it would be the first discovery of an elusive intermediate-mass black hole and, as a result, would contribute to our understanding of black hole evolution.

Acknowledgements

I would like to give my greatest thanks to Dr. Jeremy Darling. His guidance allowed me to investigate a subject I am passionate about and has made me a more confident scientist. I would especially like to thank him for being so patient in answering all my questions, encouraging me to be inquisitive, and challenging me to be a critical thinker.

I would also like to thank all the professors I had over the course of these last four years. Through very stressful semesters, they still managed to encourage my love for learning and incited my passion for observational astronomy. In particular, I want to thank Professor Glenn for introducing me to the world of research — a world that fascinates and challenges me.

My family deserves a heartfelt thank you for being so supportive of my endeavours all throughout my life. They have always encouraged me to do what I enjoy and have been my pillars of support. I thank them for always picking up the phone when I call.

I would also like to thank my friends for everything, from doing homework and eating ice cream with me to having long conversations about life. I thank Cristian for making me laugh and for putting everything in perspective for me. Without these wonderful people, I would have lost my mind a long time ago.

Finally, I sincerely thank my committee members for taking the time to read this honors thesis.

Contents

Chapter 1

Introduction

Because all galaxies in the universe contain central black holes, during galaxy mergers, the central black holes must merge as well. According to Volonteri & Perna (2005), when coalescing black holes emit gravitational waves asymmetrically, to conserve momentum, the system ejects one black hole from the galactic center. The core stars of the recoiled black hole remain bound to it as it travels out to the galaxy halo (Volonteri & Perna , 2005). This suggests that black holes populate the halos of galaxies, which are the outer, diffuse regions of galaxies and are populated by very old stars and star clusters.

The stars surrounding these black holes give scientists an indirect approach to finding recoiled black holes. Observations in the visible spectrum can provide clues that a star cluster contains a black hole. In the X-ray regime of the electromagnetic spectrum, the black hole may start accreting matter as it moves through the galaxy (Volonteri & Perna , 2005). In this case, it would appear to be an offset active galactic nucleus (AGN) (Madau & Quataert , 2004). However, accretion by a recoiled black hole would be a brief and rare occurrence. For this research, we investigated objects in the visible spectrum using SDSS and WISE magnitudes and spectroscopy.

1.1   Magnitudes

In ancient Greece, Hipparcus classified the points of light in the sky by how bright they looked to the naked eye. He used the number 1 to correspond to the brightest star, 2 for

the second brightest and so on. These assigned brightnesses are referred to as magnitudes. Today, due to advancements in science and technology, the magnitude scale ranges from -26 for the brightness of the Sun to ∼30 for the dimmest objects. It is important to note that the higher the magnitude, the less bright the object is.

Sky surveys report the magnitudes of an object in different wavelength bands. The color of an object can be determined by subtracting the magnitudes in two different wavelength bands from one another.

1.2   Optical Spectroscopy

The main technique used for this project is optical spectroscopy, which is a powerful tool in astronomy. It allows scientists to determine such characteristics of a object as distance, range of velocities (velocity dispersion) in galaxies and star clusters, age, and composition.

1.2.1   The Physics of Spectra

Quantum mechanics governs the realm of the small. According to quantum mechanics, energy is discrete. The allowed energies for an atom are given by equation 1.1

$$E_n = \frac{Z^2}{n^2} 13.6 \ eV \tag{1.1}$$

where 13.6 is the ground state energy of hydrogen, which is the amount of energy required to liberate an electron from the atom — ionization — when the electron has the lowest possible energy. The state the electron occupies is given by n and can be any integer except 0, and Z is the elements' atomic number. Equation 1.1 depends on n and demonstrates the discrete nature of allowed energies according to quantum mechanics. It's dependence on Z describes how allowed energies are unique to each element.

For emission and absorption lines to be present, the electrons in the atom must make transitions between energy levels. Absorption lines occur when incoming photons transfer energy to the electrons. This increase in electron energy causes the electron to jump to higher n. Emission lines, on the other hand, occur when the electron loses energy and transitions

to a lower n. When the electron loses energy, it emits photons with the amount of energy it has lost.

The relation $E = hc/\lambda$ relates energy to wavelength of light. In the visible spectrum (4000 Å - 7000 Å), each wavelength corresponds to a color with 4000 Å being the bluest and 7000 Å the reddest.

Because each energy level is unique to each element, the spectrum associated with an element is analogous to its fingerprint. The spectral pattern produced by an element is the same every time, unless the object is redshifted.

1.2.2   Cosmological Redshift

Since light has a finite speed of $\sim 3*10^8$ m/s, distance corresponds to time; the further away an object is, the longer its light takes to reach Earth. This means that when an object in space is observed, it is observed as it was in the past. For example, images of the Andromeda Galaxy, the closest galaxy to the Milky Way, shows it as it appeared $\sim$2.5 million years ago.

Edwin Hubble highly influenced the study of cosmology when he found that the universe is expanding. He measured the velocities of galaxies at various distances and noticed that galaxies further away were traveling faster. This is Hubble's Law and it predicts how the universe expands with time. Due to this expansion, light stretches as it travels through the universe. The increase in wavelength corresponds to a redder color. When a spectrum is redshifted, it shows the same pattern as found in the laboratory except all lines shift further into the red.

1.2.3   Viewing Spectra

A spectrometer is the instrument used to view an object's spectrum. Light from the object travels through a thin slit and hits a collimator, which is a lens that straightens the light rays. The light then hits the grating as parallel rays. The grating is a piece of glass with very thin, equally-spaced ridges and it is responsible for dispersing the light into its constituent parts. The more ridges the grating has, the higher the resolution the spectrum will have.

Another lens focuses the dispersed light and projects it onto the charged coupled device

(CCD). CCDs consist of a grid of pixels that count how many photons hit the CCD. When a photon hits a pixel, it typically has enough energy to ionize an electron. Each pixel stores the charge associated with the liberated electrons. Upon readout, the charges from each pixel are deposited in the readout register, where they are converted to voltage. The voltage goes through an analog-to-digital converter which converts from electrons to analog-to-digital units (ADU, also referred to as counts), using a conversion factor called the gain. Then the values are read out as numbers, corresponding to each pixel. In imaging, it creates an image of the object while in spectroscopy, it creates an image of the spectrum.

1.2.4   Reducing Spectra

When the CCD reports the pixel values in the form of an image, it adds a bias. The bias is a set number of ADU that is added to each pixel in order to prevent negative pixel values and to sample the read-out noise. Since these counts are not part of the science data, they are subtracted from the image. This is called bias subtraction.

The CCD also accumulates dark current, which is the ionization of electrons without the presence of a photon. Dark current is directly related to exposure time — as exposure time increases, so does the dark current. Observers often take exposures that are the same amount of time as the science exposures with the telescope shutter closed. A more efficient method is to use the edges of the image. The exposure time of the edges match that of the science data and they are untouched by incoming light.

Ultimately, the CCD is not perfect. Some parts do not respond as well to incoming light as others and so flat field images are taken. These are images of an evenly-illuminated surface to correct the science images for the change in CCD response.

This research focuses on using optical spectroscopy as a preliminary study for finding recoiled intermediate-mass black holes. A star cluster surrounding a recoiled black hole should be small due to the small size of the black hole and should exhibit features of old globular clusters in terms of color, shape and redshift (O'Leary & Loeb , 2009). Unlike globular clusters however, recoiled black hole star clusters should exhibit wide spectral lines, indicating velocities >100 km/s (O'Leary & Loeb , 2009).

O'Leary & Loeb (2012) ran N-body simulations in order to understand the distribution of stars around the black hole. Using these results and the SDSS catalogue, they presented a list of 119 candidate recoiled black holes.

This research investigates 51 of the 119 candidate recoiled black holes using optical spectroscopy. We explored two main questions.

- **Are black holes present in this sample of 51 objects?** If so, this would have implications in understanding galaxy and black hole mergers. We analyzed redshifts and types of spectra to determine if we could find an object that appeared to be a recoiled black hole.

- **Can we constrain the search criteria?** O'Leary & Loeb (2012) presented color-color criteria from SDSS for finding recoiled black holes. We wanted to know if we could further optimize the selection process and more easily remove the objects that cannot be recoiled black holes by analyzing both SDSS and WISE data.

This project is a stepping stone in the pursuit of understanding galactic evolution and black hole mergers. Although this work focuses on the Milky Way, it is possible to extend the conclusions to other galaxies in an effort to understand how galaxies and their resident black holes have evolved from the early universe to the present.

In chapter 2, we describe the observations and reductions required for the project and in chapter 3, we present the results of the redshift measurements. In chapter 4, we analyze the results and present a refined method of finding candidate black holes. Finally in chapter 5, we draw conclusions from the project, including an outline for future work.

Chapter 2

Observations and Reductions

2.1 Selection Criteria

O'Leary & Loeb (2012) ran N-body simulations to determine the distribution of stars around a recoiled black hole. These N-body simulations led to efficient search criteria including best-fit azimuthally-averaged cumulative light profiles for the simulated clusters. With this information, they created a search strategy in an effort to minimize the number of objects that cannot be recoiled black holes.

Beginning with the entirety of the Sloan Digital Sky Survey (SDSS), they first rejected all point sources, which are stars. They eliminated objects with a Petrosian radius >2". The Petrosian radius is where the integrated intensity of light within an annulus of set width is 0.2 (specific for SDSS). Their N-body results allowed them to constrain color values, which are shown in chapter 4, figures 4.1a - 4.1e. The trapezoids on these plots denote the regions in color space to search for recoiled black holes. The color constraints are given by $0.5(u-g) - 0.225 < (g-r) < 0.5(u-g) - 0.075$ and $1.25 < (u-g) < 2.75$ (O'Leary & Loeb , 2012).

Because star clusters are circular, they rejected all the objects with a ratio of semi-minor to semi-major axes of >0.7, which will eliminate edge-on spiral galaxies. To further optimize the search, they used the azimuthally-averaged cumulative light profile they found in their N-body simulations. Finally, they visually checked all remaining candidates to remove objects that were not already properly removed.

These criterion excluded all but 119 objects (O'Leary & Loeb , 2012) and Dr. Jeremy Darling observed 51 objects from this list.

2.2 Observations

The observations for this project were taken with the Apache Point Observatory (APO) Double Imaging Spectrograph (DIS) on the 3.5-m telescope with a slit width of 1.5". The grating used was the B400 with 400 lines per millimeter on the blue side and R300 with 300 lines per millimeter on the red side. These gratings were centered on wavelengths of 4398 Å in the blue and 7493 Å in the red. The linear dispersion was 1.83 Å/pix and 2.31 Å/pix on the blue and red sides, respectively.

A total of 51 objects were observed over the course of five nights ranging from July to December of 2013. The observation nights were July 8, September 7, October 9, December 10 and December 11. Most objects had three exposures for five minutes. Five of the objects had less than three exposures due to time constraints. Another four objects had six exposures due to the objects' faintness. The seeing for September 9 was 1.4", for July 8 and October 9 it was 1.5". The last two observing nights, December 10 and 11, had seeing of 1.1". Seeing refers to the turbulence of the atmosphere where the more turbulence there is, the higher the seeing and the lower the resolution.

For each night, 11 bias frames were taken. To make wavelength corrections to the science frames, we took 3 exposures of the arc lamps, containing helium, neon and argon (HeNeAr). Because the emission lines on the blue side of the CCD were more faint, we took 3 more in the blue for a longer period of time. We had a similar procedure for the Quartz lamps used for flat field corrections. Clouds appeared every night, so no standard star observations were taken for flux calibration.

2.3 Data Reduction

The observations yielded raw images of two dimensional spectra, which we reduced using Image Reduction Analysis Facility (IRAF). To start, we trimmed the edges such that only

the part of the CCD that contained our science data was reduced. The center of the CCD contains the science data and, although the edges do not contain the spectrum, they contain valuable information about the dark current and we used this to correct for the dark current in the science data.

We bias subtracted the images and flat-fielded, which did not have a large contribution to the uncertainties in line measurements (Suess , 2015). Next, to correct for the varying efficiency of detection across the CCD, we used the IRAF task, 'response'. Because flat field images exhibit the shape of the Quartz lamp spectrum, it was not possible to divide the science image by the raw flat field (Valdes , 1994). Instead, we used 'response' to fit a function to the overall shape of the flat field spectrum before we flat fielded.

To assign wavelengths to the pixels in the image, we used the 'identify' task. 'Identify' requires the user to specify the wavelength of various lines in the arclamp spectrum. Typically, we identified 10-15 lines in the blue and 30-40 lines in the red. By identifying known lines, 'identify' fits a function that maps the dispersion coordinates to the arc lamp spectrum (Valdes , 1996). This task allows for the conversion from pixel to Angstrom. We used an order 1 fit on a spline function. Next we used the IRAF task 'reidentify', which uses the wavelength solution from 'identify' as a template to fit the rest of the image to the wavelength fit. The result is a two dimensional mesh of wavelength solutions. Usually, the reidentified RMS readings were ~0.5 Å and ~0.1 Å for the red and blue sides, respectively.

The lines in the two dimensional arc lamp spectra were not perfectly straight in the spatial direction. To straighten the lines, we transformed the coordinates of the image. The task used to do this in IRAF is called 'fitcoords' and it maps how the wavelength solution changes in the spatial direction on the CCD. It required us to specify a polynomial order that would best fit the function. Usually, we used orders of 4, 5, or 6 to fit and the corners of the two dimensional spectra were off by 10-15 Å in the blue and up to 7 Å in the red.

To reduce the prevalence of cosmic rays, after coordinate transformation, we combined the images of each object using the IRAF task 'imcombine'. This task combines images by taking the median pixel value among them. Most often, three observations of five minutes were taken for each object. Some objects were observed only once due to the rising Sun or otherwise lack of time. In such cases, we did not use the 'imcombine' task.

Finally, we subtracted the emission lines from the Earth's atmosphere, as they can obscure important spectral features. IRAF's 'background' task uses an interpolation scheme to subtract out the sky lines, leaving the object's spectrum intact. 'Background' requires the user to input a range of pixel values that are interpolated over. We typically used the 1100-1300 pixel range because it encompassed many night sky lines over which to interpolate. Because the sky emission lines are so bright and interpolation is not perfect, the night sky lines often leave visible remnants on the spectrum of interest as well as the background. If these remnants are too distracting, we background subtracted each frame in the set and then combined them. This lessens the effect these poorly subtracted skylines have on the science spectrum. We did this for ∼1/3 of the objects.

Because it was easier to view the final image as a one dimensional spectrum, we used the IRAF task 'apall.' This task requires the user to define an aperture that communicates to 'apall' which pixels to look at in the linear direction when plotting the one dimensional spectrum. Then we set the trace which informs 'apall' how the spectrum moves in the spatial direction as it progresses in the spectral direction.

2.4   Line Measurement

We used the IRAF task 'splot' to view the one dimensional spectra. In order to more easily identify features of the spectrum, we used smoothing with a three pixel boxcar. This reduced the noise while making the real features more prominent. Due to the redshifts of many of the observed objects, typically the only line found on the blue side was the 3727 Å [OII] line. On the redside, the Balmer line of Hα was the most visible, with [NII] lines on either side. Often the [SII] doublet occured further into the red and the [OIII] lines with rest wavelengths of ∼5007 Å and ∼4959 Å as well as Hβ appeared on the blue side of Hα.

To get the best estimate of line uncertainties, we measured the RMS of circular regions in the final two dimensional image in DS9. These regions were selected such that they were clear of any spectrum and poorly subtracted night sky lines. We gave the RMS value to 'splot' so that it could be taken into account when the program calculated line uncertainties. Typical values of the RMS in one of these regions were between 1 and 3 counts. The typical

value of 1.8 was passed to 'splot'. When we measured the line wavelengths, 'splot' also reported an uncertainty, taking into account the fit it used as well as the RMS value it was given.

2.5   Uncertainty Calculations

We used the line uncertainties reported by 'splot' to compute the uncertainties in redshift. The linear dispersion for APO DIS is 125 km/s. Next, we used the standard uncertainty equation given by equation 2.1

$$\sigma_f^2 = \left(\frac{\partial f}{\partial x}\right)^2 \sigma_x^2 + \left(\frac{\partial f}{\partial y}\right)^2 \sigma_y^2 \tag{2.1}$$

where f is a function of x and y. More specifically, f is the redshift equation (equation 2.2), which is a function of λ_{obs} and λ_{rest}. We converted the line centroid uncertainty to redshift uncertainty, using equation 2.3

$$z = \left(\frac{\lambda_{obs}}{\lambda_{rest}}\right) - 1 \tag{2.2}$$

$$\sigma_{z_i} = \frac{\sigma_{\lambda_{obs_i}}}{\lambda_{rest_i}} \tag{2.3}$$

Because there were redshift measurements for each spectral line found, we used a weighted average (equation 2.4) to calculate the final redshifts with the weights given in equation 2.5.

$$z = \frac{\sum\limits_i w_i z_i}{\sum\limits_i w_i} \tag{2.4}$$

$$w_i = \frac{1}{\sigma_{z_i}^2} \tag{2.5}$$

To find the centroid uncertainty, we applied equation 2.1 to equation 2.4 and equation 2.6 is the result.

$$\sigma_z = \sqrt{\frac{1}{\sum\limits_i w_i}} \tag{2.6}$$

Lastly, we added this result and the linear dispersion in quadrature. Converting the linear dispersion from velocity ($\sim$125 km/s) to redshift, we found that it corresponds to a redshift of $\sim$0.00042. When we added this with the centroid uncertainty in quadrature, the linear dispersion dominated. Another source of very small uncertainty is that from 'fitcoords'. However, because the uncertainty that 'fitcoords' introduces is so small, we can neglect it.

The redshifts and corresponding uncertainties are presented in Chapter 3.

Chapter 3

Results of Redshift Determination

One question we asked was whether one of the 51 observed objects is a recoiled black hole. We sorted the objects into four categories based on spectral features and redshift measurements. The first category included objects with emission lines. For this project, we were interested in objects that looked like globular clusters. Globular clusters are old, red and do not contain gas or dust. Emission lines suggest otherwise and, depending upon the redshift, the object can be classified as a galaxy. Such was the case with most of the observed objects. We classified few objects as continuum-only, displaying no distinguishable emission or absorption lines. One object which was categorized as continuum-only displays what appears to be the 4000 Å break. This feature occurs at ~4000 Å and is characterized by a sharp jump in the continuum with calcium H and K (3968 Å and 3934 Å) lines at the lower end. In such cases, it was possible to determine its redshift. We specified other objects as continuum-only because they do not exhibit absorption or emission lines. The lack of spectral features could indicate that the signal-to-noise ratio was too low to observe spectral features. Despite the reason for lacking spectral lines, they still have unknown redshifts.

It was also possible to find absorption line spectra. The spectra of ellipticals and globular clusters contain many absorption lines due to the spectra of the old stars therein. In this project, we were most interested in absorption line spectra with z~0 however, we did not identify objects with obvious absorption lines.

In some cases, an object's spectrum displayed inconclusive features. Often this was because the possible emission or absorption lines were not distinct enough to definitively

conclude that they were real lines; instead they may have been poorly-subtracted sky lines or portions of high noise. These were categorized as ambiguous, as they could still be emission or absorption line spectra or continuum-only. In few cases, ambiguous spectra were classified as such because they were too faint, even after combining the set of images. We recommend further observations to definitively conclude the categorization of these objects.

Because the objects of interest were globular clusters in the halo of the Milky Way, the most convincing objects have a redshift of $\sim$0 and an absorption spectrum. We determined all redshifts to be larger than 0.05 and none to be absorption line spectra (refer to Table 3.1). Thus, none of the objects for which we identified redshifts are in the galaxy and therefore, none are the recoiled black holes we seek.

3.0.1 Notes on specific objects

We found objects with interesting features that are worth noting.

SDSS J003209.31+071259.2

This object has a large absorption feature spanning $\sim$200 Å. Originally, we suspected it to be Lyman-α absorption, suggesting a high redshift. However, upon further inspection, it became clear that much of the 200 Å feature was due to noise. Although we determined that this is not Lyman-α absorption, this may be an absorption feature of some sort. We classified this as ambiguous because, although this may be a feature, we have no context to indicating what that feature is.

SDSS J064325.65+281559.3

The SDSS magnitudes for this object may be incorrect. We viewed the SDSS finder chart for this object and it appears it was not observed in all wavelength bands. The reported magnitudes may suggest that the object is redder than it actually is because of this. Figure 3.1 is a thumbnail from SDSS of this object and the surrounding area.

Figure 3.1 This thumbnail of SDSS J064325.65+281559.3 shows that the object of interest and the surrounding objects are all very red, indicating that these objects were not surveyed in all SDSS filters.

SDSS J090546.22+225309.9

In the two dimensional spectrum, the Hα line was wide and easily seen. The one dimensional spectrum confirmed the wide line is, in fact, a single emission line with narrow bracketing nitrogen lines. These features are clear signs of an active galactic nucleus (AGN). Figure 3.2 shows the spectrum of this object
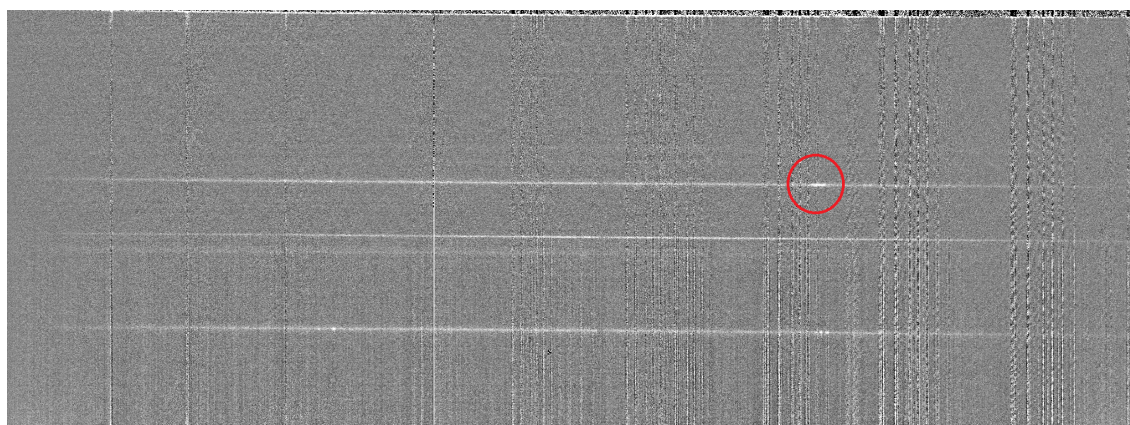
Figure 3.2 The final reduced spectrum of SDSS J090546.22+225309.9, where the broadened Hα line is visible in the red circle. Other emission lines are also visible across the spectrum.

SDSS J100310.59+282625.0

The spectrum of this object shows an obvious step at $\sim$4315 Å. This suggests that it could be the 4000 Å break if it is at a redshift of $\sim$0.079. However, there were no obvious calcium H and K absorption lines at the bottom of the break. We have included the redshift in Table 3.1 but the uncertainty is very large.

Table 3.1. The measured redshifts for each object resulting from line identification as well as the object categorization.

Object Name	Redshift	Categorization
SDSS J003209.31+071259.2	-	Ambiguous
SDSS J003550.53-100543.0	0.1612(4)	Emission
SDSS J005248.49+155331.6	0.2564(4)	Emission
SDSS J011023.54-090416.1	0.1663(4)	Emission
SDSS J015724.63-085424.1	0.0500(4)	Emission
SDSS J020705.55+003738.9	0.1524(4)	Emission
SDSS J021500.57+001217.8	0.2891(4)	Emission
SDSS J030347.44-081909.5	0.2642(4)	Emission
SDSS J045505.26+244156.3	-	Continuum
SDSS J051413.98+164920.2	-	Ambiguous
SDSS J052222.65-013302.9	0.2098(4)	Emission
SDSS J064325.65+281559.3	-	Ambiguous
SDSS J073940.32+221323.1	0.0761(4)	Emission
SDSS J074214.49+251424.0	0.2434(4)	Emission
SDSS J074827.56+261836.6	0.2014(4)	Emission
SDSS J075550.27+343959.3	0.2066(4)	Emission
SDSS J080005.57+514410.6	0.3829(4)	Emission
SDSS J081020.09+315018.6	0.3242(4)	Emission
SDSS J081546.83+155039.8	0.1263(4)	Emission
SDSS J082724.19+340543.7	0.0727(4)	Emission
SDSS J083158.70+332233.5	0.1407(4)	Emission
SDSS J083701.15+230023.2	0.1285(4)	Emission
SDSS J084034.69+162319.5	0.2039(4)	Emission
SDSS J084246.26+361533.7	0.2762(4)	Emission
SDSS J084505.56+451932.0	0.0544(4)	Emission
SDSS J084647.94+001638.4	0.1564(4)	Emission
SDSS J084822.47+355630.4	0.1180(4)	Emission
SDSS J090546.22+225309.9	0.2957(4)	Emission
SDSS J092335.02+472837.1	0.1727(4)	Emission

Table 3.1 (cont'd)

Object Name	Redshift	Categorization
SDSS J092607.17+021555.4	-	Ambiguous
SDSS J092757.48+054543.7	0.1875(4)	Emission
SDSS J092921.02+545144.3	0.1342(4)	Emission
SDSS J100310.59+282625.0	0.079:*	Continuum
SDSS J101754.64+803827.9	0.2334(4)	Emission
SDSS J104012.45+645611.0	-	Ambiguous
SDSS J104700.20+451459.4	0.2343(4)	Emission
SDSS J102509.23+215445.8	-	Ambiguous
SDSS J105846.93+170430.1	0.1162(4)	Emission
SDSS J105907.75-031445.6	-	Ambiguous
SDSS J150113.32+051304.1	0.2490(4)	Emission
SDSS J155333.07+423146.0	-	Ambiguous
SDSS J155442.55+055111.1	0.1025(4)	Emission
SDSS J160236.41+322318.7	-	Ambiguous
SDSS J160630.13+351046.2	0.1211(4)	Emission
SDSS J163339.50+440918.3	-	Ambiguous
SDSS J163659.29+235816.2	-	Ambiguous
SDSS J170525.39+235241.5	-	Ambiguous
SDSS J210803.13-001350.4	0.0951(4)	Emission
SDSS J213035.54-070545.7	-	Ambiguous
SDSS J215424.98+002023.4	0.2224(4)	Emission
SDSS J233106.11+075810.9	0.3004(4)	Emission

*The colon indicates that the measured redshift is not well-known. The 4000 Å break is often rounded to 4000 Å and the exact location of the break in a spectrum is not standardized.

Chapter 4

Refined Method for Finding Candidate Recoiled Black Holes

Most of the objects observed for this research are galaxies. Although we did not find recoiled black holes in our sample of 51 objects, we can still present refined parameters for identifying objects to observe. In the future, these refined parameters will further optimize the selection process.

We did not exclude the ambiguous objects when analyzing the data. Since we have not definitively classified them, it is still possible that they are recoiled black holes.

We divided the objects into two categories — those we can eliminate as recoiled black holes and those we cannot. Among those that we eliminated from the list are those with emission lines and high redshift. Among those we included are the ambiguous spectra and absorption line spectra, if there were any present, with low redshift. We used the Kolmogorov-Smirnov (KS) test to determine whether the two populations originate from the same parent distribution.

4.1 Kolmogorov-Smirnov Test

The KS test is a measure of the probability that two populations originate from the same parent distribution however, it does not require prior knowledge of the populations' parent distribution. In this research, we used the two-sample KS test to test whether the objects that

are possible recoiled black holes and those that are not are drawn from the same distribution.

The KS test calculates two values — the D-statistic and the P value. The D-statistic reports the difference between the cumulative distribution functions (CDF) and is given by equation 4.1

$$D = Max(|F_1 - F_2|) \tag{4.1}$$

where F_1 and F_2 are the CDFs of the comparison populations. The smaller the D-statistic, the more likely they are drawn from the same distribution. In this work, we do not report the D-statistic because it is heavily influenced by fluctuations in the individual populations' values.

The P value reveals whether or not we can reject the null hypothesis, which states that the two comparison populations are from the same parent distribution. We chose the 99% significance level for this research. If the P value is < 0.01, we can conclude that the two populations are inconsistent with the null hypothesis (i.e., that they are drawn from different distributions). Rejection of the null hypothesis allows us to further constrain the magnitudes and colors of objects that we observe in an effort to optimize the search process.

4.2   Sloan Colors and Magnitudes

O'Leary & Loeb (2012) presented the criteria for candidate black holes, using data from SDSS Data Release 7. SDSS is an all-sky survey using the Sloan Foundation 2.5-m Telescope, located at Apache Point Observatory. It made advancements in the field of cosmology by mapping the overall structure of the observable universe. SDSS uses 5 filters when imaging the sky — u, g, r, i and z — spanning from ultraviolet (u) to infrared (z).

In order to refine the SDSS search criteria, we recreated the color-color plots from O'Leary & Loeb (2012) and further investigated relationships between other Sloan colors and magnitudes. Many of the observed objects had reported magnitudes dimmer than the SDSS magnitude limit in the u band and one object was limited in the z band. In these cases, we used the limiting magnitude (22.0 and 20.5 for the u and z bands, respectively) instead of the reported magnitudes. Table 4.1 reports the results of the KS tests for SDSS magnitudes

and colors. At the 99% significance level, the colors $(u - g)$, $(g - r)$, and $(r - i)$ are drawn from different parent distributions. As shown in figures 4.1a, 4.1c and 4.1e, there are noticeable differences between the distributions of identified redshifts and unidentified redshifts. However, when performing the KS test on $(u - g)$, $(i - z)$, u and z, we excluded the objects with magnitude upper limits.

Due to the limits of many of our sources in the u band, the uncertainties on u and $(u - g)$ are very large. We know that magnitudes in the u band are not well-constrained; the typical uncertainty is ~ 0.8 in u, while the typical uncertainty in the i and r bands is > 0.1 and ~ 0.2 for the z band. This calls into question the legitimacy of using $(u - g)$ to constrain the search criteria. Figure 4.1a shows that the uncertainty in $(u - g)$ spans almost the entire plot. Due to these large uncertainties, we cannot confidently conclude that $(u - g)$ should be used to optimize the search process.

In $(g - r)$, remaining candidate black holes are above ~ 0.6, for $(r - i)$, they are above ~ 0.3. Because of the inverted nature of the magnitude system, this tells us that these objects are redder than those with emission lines. Fortunately, recoiled black holes exhibit these characteristics and this allows us to even better constrain search criteria for candidate black holes.

The SDSS magnitude values used in this analysis are in Table 4.2

(a)

(b)

(c)

(d)

(e)
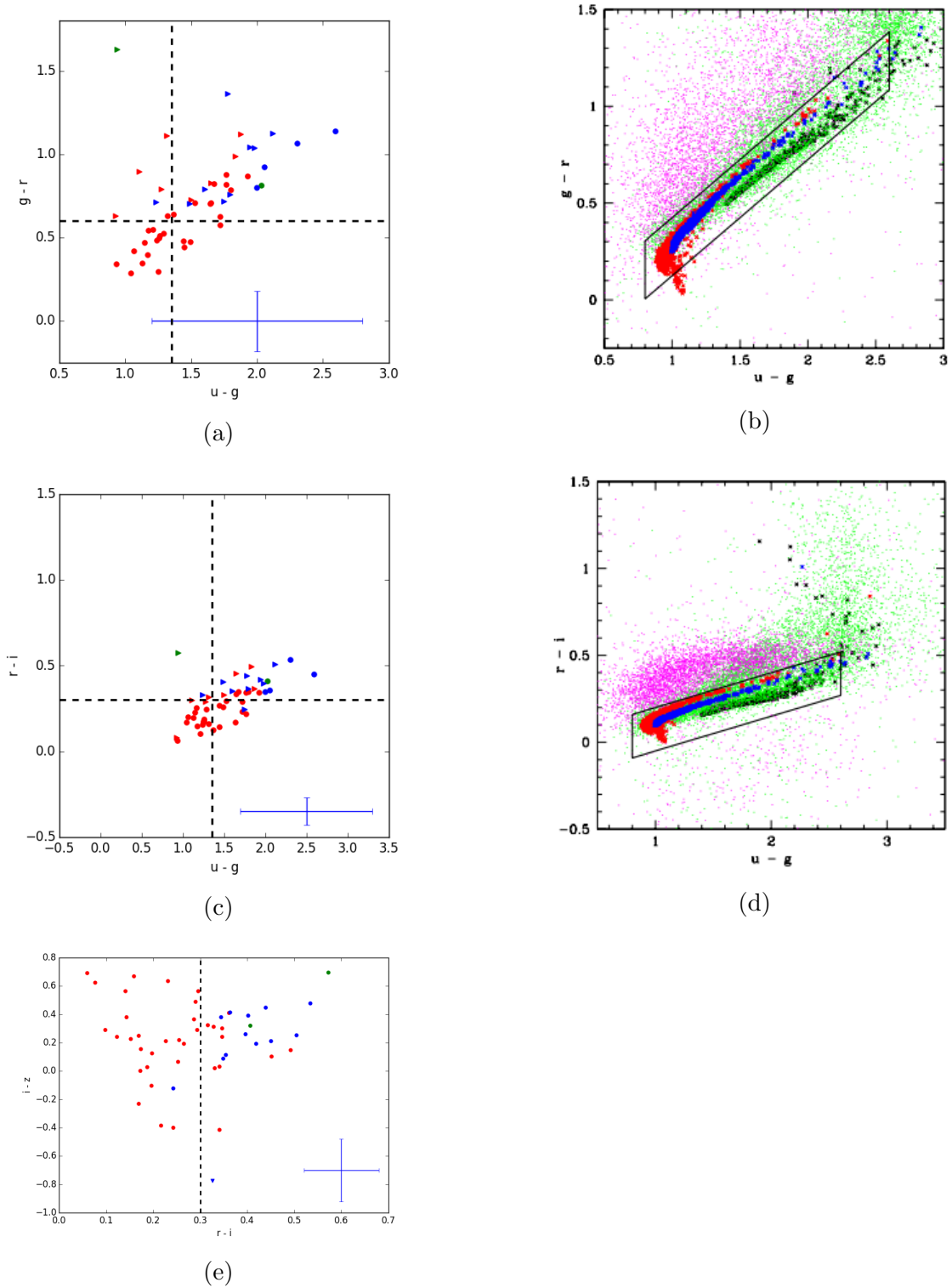
Figure 4.1 (a), (c) and (f) show the parameters that are statistically significant, according to the KS test. The triangle symbols represent the objects with reported magnitudes larger than SDSS limiting magnitude. (b) and (d) are figures 9(a) and 9(b) in O'Leary & Loeb (2012). In (a), (c) and (f), the blue symbols are ambiguous spectra, the green symbols represent continuum-only objects and the red symbols are emission line spectra

23

4.3 WISE Colors and Magnitudes

The Wide-Field Infrared Explorer (WISE) was a mission launched in 2009. According to Wright et al. (2010), the data gathered contributes to research in star formation, asteroids, and interstellar dust, among other topics . In six months, it observed the entire sky in the infrared in four wavelength bands—3.4, 4.6, 12, and 22 microns (Wright et al. , 2010). We cross-referenced our observed objects with those in the WISE Survey. Out of the 51 objects we observed, WISE detected 43 of them in one or more band.

Of these object, 33 of them had 12 micron band detections with signal-to-noise ratios that were too small to definitively consider them detections. If the 12 micron detection had a signal-to-noise ratio of less than 4, we disregarded the reported detection magnitude and used the limiting magnitude of 12.5 as the detected magnitude. This is reflected in figure 4.2b, where the left-pointing triangles means that $[4.6] - [12]$ could be any value at that point or lower. On figure 4.2b, the blue symbols correspond to ambiguous spectra, the green symbols represent objects with a continuum and the red symbols are emission line spectra.
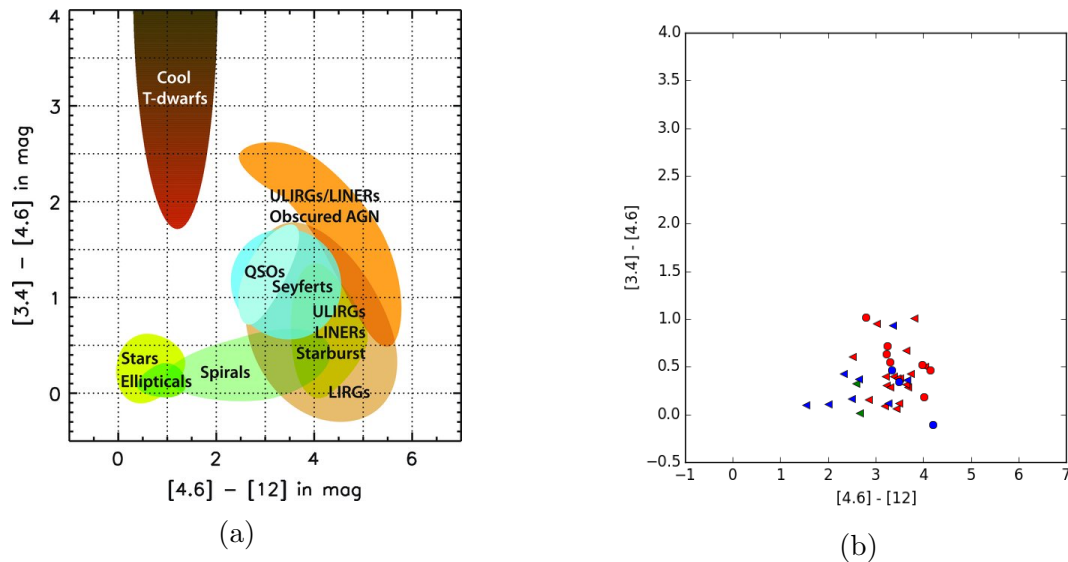
Figure 4.2 (a) is from Wright et al. (2010) to show the correspondence between WISE color and object. (b) is a WISE color-color plot for our observed objects. The object that is closest to the "Stars" and "Ellipticals" regions is SDSS J151413.98+164920.2.

Wright (2010) presented Figure 4.2a which shows the locations of objects on a WISE color plot. Figures 4.2a and 4.2b can help identify the kinds of objects the ambiguous spectra are.

We hoped to see ambiguous detections lie in the parts of the diagram labelled "Stars" and "Ellipticals". Only one is located close to these regions — SDSS J0151413.98+164920.2. The locations of the emission line spectra in this plot confirm our conclusions that many of them are spiral galaxies.

We calculated the KS test for the WISE detections much like we did for SDSS. These results are presented in Table 4.1 and the WISE magnitudes used for this analysis are presented in Table 4.3. The WISE data does not further constrain the search parameters.

	Parameter	P Value
Sloan Colors	**u - g**	**7.70e-4**
	g - r	**1.17e-3**
	r - i	**4.14e-5**
	i - z	0.693
Sloan Magnitudes	u	0.279
	g	0.749
	r	0.263
	i	0.048
	z	0.016
WISE colors	[3.4] - [4.6]	0.174
	[4.6] - [12]	0.340
WISE Magnitudes	[3.4]	0.019
	[4.6]	0.063

Table 4.1 KS test results for SDSS and WISE magnitudes and colors. The bold values are statistically significant. We can further constrain the search criteria with the SDSS colors.

Table 4.2. The SDSS magnitudes used in the SDSS color-color plots and their uncertainties.

Object Name	u	g	r	i	z
SDSS J003209.31+071259.2	21.54(1.02)	18.94(03)	17.80(03)	17.35(02)	17.14(06)
SDSS J003550.53-100543.0	21.07(47)	19.57(04)	19.10(03)	18.85(06)	18.63(22)
SDSS J005248.49+155331.6	21.49(55)	19.81(05)	18.99(02)	18.65(04)	18.40(12)
SDSS J011023.54-090416.1	20.87(40)	19.70(05)	19.31(04)	19.05(08)	18.99(28)
SDSS J015724.63-085424.1	19.74(16)	18.48(02)	18.19(02)	18.01(03)	18.01(14)
SDSS J020705.55+003738.9	21.11(48)	19.81(06)	19.29(03)	19.05(07)	19.45(33)
SDSS J021500.57+001217.8	21.77(1.01)	20.40(09)	19.77(05)	19.64(11)	19.40(44)
SDSS J030347.44-081909.5	22.25(1.25)*	20.12(07)	19.01(04)	18.65(04)	18.24(12)
SDSS J045505.26+244156.3	24.02(4.35)*	21.06(14)	19.43(05)	18.86(04)	18.17(08)
SDSS J051413.98+164920.2	21.26(51)	18.95(15)	17.89(10)	17.36(08)	16.88(07)
SDSS J052222.65-013302.9	22.51(1.33)*	20.16(05)	19.18(03)	18.68(03)	18.53(10)
SDSS J064325.65+281559.3	22.36(97)*	20.51(06)	19.81(06)	19.40(06)	19.01(21)
SDSS J073940.32+221323.1	19.72(16)	18.67(02)	18.39(02)	18.22(04)	18.45(19)
SDSS J074214.49+251424.0	21.94(75)	20.14(06)	19.35(03)	19.01(05)	18.71(11)
SDSS J074827.56+261836.6	21.39(57)	19.74(04)	19.04(03)	18.71(04)	18.69(16)
SDSS J075550.27+343959.3	21.84(66)	20.51(08)	19.89(06)	19.73(11)	19.06(23)
SDSS J080005.57+514410.6	22.85(2.33)*	20.68(11)	19.57(04)	19.26(08)	18.93(24)
SDSS J081020.09+315018.6	22.43(1.08)*	20.72(09)	19.93(07)	19.64(08)	19.15(15)
SDSS J081546.83+155039.8	21.77(62)	20.32(06)	19.88(06)	19.74(09)	19.17(27)
SDSS J082724.19+340543.7	20.95(35)	19.77(05)	19.23(04)	19.09(05)	18.71(14)
SDSS J083158.70+332233.5	20.50(20)	19.35(03)	18.89(02)	18.66(03)	18.45(13)
SDSS J083701.15+230023.2	21.48(42)	20.54(07)	20.20(08)	20.14(12)	19.45(22)
SDSS J084034.69+162319.5	21.39(42)	20.13(05)	19.62(04)	19.44(08)	19.29(24)
SDSS J084246.26+361533.7	21.38(72)	19.66(05)	19.09(04)	18.86(05)	18.22(10)
SDSS J084505.56+451932.0	21.83(65)	20.59(12)	20.11(07)	19.95(13)	19.73(38)
SDSS J084647.94+001638.4	22.42(96)*	21.07(12)	20.44(10)	20.36(19)	19.74(39)
SDSS J084822.47+355630.4	20.13(19)	18.69(02)	18.21(02)	17.95(02)	17.75(09)
SDSS J090546.22+225309.9	22.29(82)*	20.50(07)	19.77(07)	19.44(06)	19.13(22)
SDSS J092335.02+472837.1	21.36(50)	19.64(03)	19.01(02)	18.73(03)	18.36(09)

Table 4.2 (cont'd)

Object Name	u	g	r	i	z
SDSS J092607.17+021555.4	22.16(1.16)*	20.39(10)	19.60(07)	19.25(09)	19.17(30)
SDSS J092757.48+054543.7	21.80(80)	20.03(05)	19.22(04)	18.88(05)	18.85(21)
SDSS J092921.02+545144.3	20.44(19)	19.31(03)	18.97(03)	18.77(04)	18.87(21)
SDSS J100310.59+282625.0	20.89(28)	18.86(02)	18.05(02)	17.64(02)	17.32(05)
SDSS J101754.64+803827.9	21.79(1.17)	20.02(06)	19.14(03)	18.93(07)	19.31(47)
SDSS J104012.45+645611.0	22.01(97)	20.21(06)	19.45(06)	19.08(06)	18.67(16)
SDSS J104700.20+451459.4	21.59(63)	19.95(05)	19.24(03)	19.07(05)	18.82(21)
SDSS J102509.23+215445.8	22.80(2.09)*	20.22(07)	18.86(03)	18.42(04)	17.97(09)
SDSS J105846.93+170430.1	20.61(29)	19.07(03)	18.37(02)	18.07(03)	17.79(08)
SDSS J105907.75-031445.6	21.65(57)	19.60(05)	18.67(03)	18.32(03)	18.20(10)
SDSS J150113.32+051304.1	21.14(42)	19.92(05)	19.38(04)	19.28(06)	18.99(19)
SDSS J155333.07+423146.0	22.12(98)*	20.25(06)	19.53(05)	19.29(06)	19.41(28)
SDSS J155442.55+055111.1	20.35(24)	19.09(03)	18.60(02)	18.41(03)	18.38(13)
SDSS J160236.41+322318.7	22.41(92)*	19.88(04)	18.75(02)	18.25(03)	18.00(08)
SDSS J160630.13+351046.2	20.55(20)	19.48(03)	19.06(03)	18.87(04)	18.74(16)
SDSS J163339.50+440918.3	22.14(82)*	20.02(04)	18.98(03)	18.59(03)	18.33(11)
SDSS J163659.29+235816.2	22.34(1.20)*	20.05(05)	19.01(03)	18.59(03)	18.40(12)
SDSS J170525.39+235241.5	21.17(59)	19.17(03)	18.37(02)	18.03(03)	17.65(09)
SDSS J210803.13-001350.4	22.39(1.44)*	20.35(09)	19.52(05)	19.07(06)	18.97(25)
SDSS J213035.54-070545.7	22.37(1.59)*	20.76(13)	20.05(08)	19.72(12)	20.53(1.27)*
SDSS J215424.98+002023.4	21.94(1.01)	20.01(06)	19.14(03)	18.80(05)	19.22(35)
SDSS J233106.11+075810.9	22.65(1.63)*	20.89(12)	19.99(06)	19.70(11)	19.13(24)

*Reported magnitudes are dimmer than Sloan magnitude limits. $u_{lim} = 22.0$, $g_{lim} = 22.2$, $r_{lim} = 22.2$, $i_{lim} = 21.3$, $z_{lim} = 20.5$

Table 4.3.   The WISE magnitudes we used in our analysis and their uncertainties

Object Name	[3.4]	[4.6]	[12]
SDSS J003209.31+071259.4	14.614(036)	14.500(074)	11.787(000)*
SDSS J003550.52-100542.6	16.387(101)	16.007(253)	11.968(000)*
SDSS J005248.47+155331.9	15.578(050)	14.942(079)	1.719(188)
SDSS J011023.51-090415.2	16.476(080)	16.184(235)	12.776(510)*
SDSS J015724.62-085424.2	16.001(066)	15.940(201)	12.784(531)*
SDSS J020705.51+003742.0	16.409(073)	15.948(159)	11.806(169)
SDSS J021500.56+001216.9	17/323(161)	16.313(229)	12.698(414)*
SDSS J030347.44-081909.1	15.140(033)	14.418(048)	11.177(084)*
SDSS J045505.26+244156.2	15.416(063)	15.091(129)	12.344(000)*
SDSS J051413.99+164920.6	14.145(032)	14.045(054)	12.513(000)*
SDSS J052222.65-013303.6	15.628(058)	15.018(097)	12.359(000)*
SDSS J064325.59+281559.3	16.633(136)	16.420(487)*	11.504(000)*
SDSS J073940.33+221323.7	16.267(094)	15.871(221)	12.644(000)*
SDSS J074214.50+251424.1	16.257(085)	15.731(183)	11.750(237)
SDSS J074827.52+261837.1	16.484(109)	15.528(152)	12.173(393)*
SDSS J080005.58+514410.7	15.679(054)	15.125(094)	11.820(214)
SDSS J081020.10+315018.6	16.593(115)	16.566(379)*	12.601(498)*
SDSS J081546.83+155040.0	17.433(200)	16.705(000)*	12.816(000)*
SDSS J083158.72+332233.0	16.025(072)	15.720(195)	12.069(294)*
SDSS J084246.24+361533.5	16.100(080)	15.701(170)	12.169(343)*
SDSS J084822.44+355630.4	15.781(060)	15.689(168)	12.635(475)*
SDSS J090546.23+225310.0	15.021(041)	14.005(047)	11.211(141)
SDSS J092335.01+472836.9	16.087(059)	15.799(141)	12.524(363)*
SDSS J092607.14+021555.2	16.787(132)	15.849(199)	12.274(000)*
SDSS J092757.49+054544.0	16.325(091)	15.947(220)	12.578(000)*
SDSS J092921.00+545144.1	16.833(123)	16.461(304)*	12.532(000)*
SDSS J100310.61+282625.1	15.166(045)	15.154(111)	12.180(000)*
SDSS J101754.46+803828.0	16.192(061)	16.010(155)	11.992(181)
SDSS J102509.18+215446.4	15.252(042)	14.828(071)	12.360(000)*

Table 4.3 (cont'd)

Object Name	[3.4]	[4.6]	[12]
SDSS J104012.50+645611.3	16.522(083)	16.163(198)	12.460(000)*
SDSS J104700.20+451459.6	16.458(090)	16.145(234)	12.571(408)*
SDSS J105846.93+170430.0	15.508(054)	15.355(142)	12.090(000)*
SDSS J105907.77-031445.6	15.173(043)	14.705(073)	11.375(142)
SDSS J150113.31+051304.1	17.041(115)	16.536(246)	12.829(394)*
SDSS J155333.10+423146.0	16.831(076)	16.935(267)	12.735(260)
SDSS J155442.52+055111.5	15.995(070)	16.404(316)*	12.359(375)*
SDSS J160236.43+322318.6	15.157(032)	14.992(059)	13.389(000)*
SDSS J160630.11+351047.5	16.659(067)	16.228(148)	12.839(000)*
SDSS J163339.51+440918.4	15.873(052)	15.758(135)	12.892(409)*
SDSS J163659.29+235816.5	15.568(048)	15.222(092)	11.733(171)
SDSS J170525.37+235241.7	15.527(048)	15.152(093)	12.896(000)*
SDSS J215425.00+002023.6	16.107(074)	15.991(230)	12.193(000)*
SDSS J233106.06+075811.3	16.800(138)	16.130(241)	12.524(000)*

*Reported signal-to-noise ratios of WISE detection for object is less than 4.

Chapter 5

Conclusions

O'Leary & Loeb (2012) ran simulations to determine the appearance of recoiled black holes in observations. Using the results of these simulations, they detailed criteria for the appearance of objects to be observed. They searched through SDSS DR7 with these criteria and presented a list of 119 objects that fit their specifications.

Out of these 119 candidate black holes, Dr. Jeremy Darling observed 51 of them using DIS at APO over the course of five nights in 2013. After reducing the spectra in IRAF, we measured redshifts for the objects with spectral features. All identified redshifts were large and they were usually emission line spectra, suggesting the object is a galaxy. The two continuum-only objects could mean that the signal-to-noise ratio was too low to observe absorption or emission lines. For this project, we were most interested in objects that have a low redshift and display absorption lines, showing that the object is old and located in the Milky Way. Candidate black holes would also be nearly undetected in the WISE 12 and 22 micron bands, indicating a lack of dust.

Next, we looked at a variety of trends using SDSS and WISE. SDSS colors allowed us to remove objects that are not recoiled black holes. Specifically, after running the KS test on the $(u-g)$, $(g-r)$ and $(r-i)$ Sloan colors, we concluded that there was a difference between the populations of objects that are not recoiled black holes and those that may be. However, the large uncertainties in the u band make it difficult to constrain the $(u-g)$ parameters and so may not be helpful in optimizing the search. WISE did not reveal any informative trend to further constrain search criteria.

5.1 Future Work

In the future, we recommend using the criteria presented by O'Leary and Loeb (2012) as well as implementing the following restrictions:

- $(g - r) \geq 0.6$

- $(r - i) \geq 0.3$

Using these restrictions, the remaining 68 objects from O'Leary & Loeb (2012) can be narrowed down to 21. These objects are in Table 5.1.

We found 13 ambiguous objects but there are a variety of ways to clarify the nature of these objects in the future. We recommend using a larger telescope to increase the light-collecting area and, as a result, produce a spectrum with a higher signal-to-noise ratio, making spectral features more prominent. Another option is to increase the exposure time. We typically observed each object three times for five minutes. By increasing the exposure time, the amount of light collected by the CCD increases, which will also result in a spectrum with higher signal-to-noise.

If a candidate recoiled black hole is found, we suggest observing it with a higher resolution grating. In our case, we used the lowest resolution grating because we were interested in finding emission and absorption lines only, as a preliminary study. With higher resolution, it is possible to measure the velocity dispersion of the stars in the object, as evidenced by wide emission and absorption lines. It would also be helpful to determine the mass-to-light ratio of the object. If the velocity dispersion is larger than ~ 100 km/s and the mass-to-light ratio is large, we can conclude that a massive body is lurking at the center.

We answered both questions we set out to answer; we did not find evidence of recoiled black holes in our set of 51 objects but we were able to constrain the SDSS color criteria. This will help future researchers more efficiently find a black hole shrouded in stars, wandering about the Milky Way's halo.

Table 5.1. Implementing the restrictions $(g-r) \geq 0.6$ and $(r-i) \geq 0.3$, we reduce the number of remaining sources to be observed, given in O'Leary & Loeb (2012), from 68 to 21.

Object Name	$g-r$	$r-i$
SDSS J093815.82+231234.8	0.91	0.39
SDSS J105840.27 - 012816.9	0.82	0.34
SDSS J112711.19+113814.8	0.89	0.30
SDSS J113308.62+002113.2	1.14	0.50
SDSS J115253.98+171842.6	0.73	0.36
SDSS J120533.94+022352.9	0.85	0.38
SDSS J121414.73+161215.4	0.93	0.42
SDSS J123544.93+193016.9	0.69	0.34
SDSS J125011.62 - 021800.1	0.65	0.35
SDSS J125958.63 - 002508.4	1.04	0.37
SDSS J132908.57+232303.8	1.16	0.46
SDSS J134127.13+081550.6	1.04	0.33
SDSS J135018.11+092421.7	0.99	0.39
SDSS J135241.53+121430.8	0.84	0.32
SDSS J141327.28+282847.1	0.79	0.34
SDSS J144115.60+185843.8	0.86	0.33
SDSS J144856.99+153744.6	0.85	0.31
SDSS J145345.50+080808.7	0.79	0.40
SDSS J152006.92+085031.0	0.77	0.33
SDSS J152646.00+210607.1	1.25	0.48
SDSS J162536.57+563531.9	1.03	0.34

Bibliography

Campanelli, M., Lousto, C. O., Zlochower, Y., & Merritt, D. (2007). Maximum Gravitational Recoil. Physical Review Letters, 98(23), 231102. http://doi.org/10.1103/PhysRevLett.98.231102

Madau, P., & Quataert, E. (2004). The effect of gravitational-wave recoil on the demography of massive black holes. The Astrophysical Journal, 606(1), L17–L20. http://doi.org/10.1086/421017

O'Leary, R. M., & Loeb, A. (2009). Star Clusters Around Recoiled Black Holes in the Milky Way Halo. Monthly Notices of the Royal Astronomical Society, 395(2), 781–786. http://doi.org/10.1111/j.1365-2966.2009.14611.x

O'Leary, R. M., & Loeb, A. (2012). Recoiled star clusters in the Milky Way halo: N-body simulations and a candidate search through the SDSS. Monthly Notices of the Royal Astronomical Society, 421(4), 2737–2750. http://doi.org/10.1111/j.1365-2966.2011.20078.x

Petrosian, V. (1976). Surface brightness and evolution of galaxies. Astrophysical Journal. http://doi.org/10.1086/182253

Suess, K. (2015). Identifying OH Imposters in the ALFALFA Neutral Hydrogen Survey. Undergraduate Honors Theses. Retrieved from http://scholar.colorado.edu/honr_theses/805

Valdes, F. (1994). IRAF Tutorials: extraction of stellar long slit spectra using doslit. Retrieved September 22, 2015.

Valdes, F. (1996). Automated Arc Line Identifications in IRAF. Retrieved September 22, 2015.

Volonteri, M., & Perna, R. (2005). Dynamical evolution of intermediate mass black holes and their observable signatures in the nearby Universe. Monthly Notices of the Royal Astronomical Society, 358(3), 913–922. http://doi.org/10.1111/j.1365-2966.2005.08832.x

Wright, E. L., Eisenhardt, P. R. M., Mainzer, A. K., Ressler, M. E., Cutri, R. M., Jarrett, T., . . . Tsai, C.-W. (2010). The Wide-Field Infrared Survey Explorer (WISE): Mission descriptiono and initial on-orbit performance. The Astronomical Journal, 140(6), 1868–1881. http://doi.org/10.1088/0004-6256/140/6/1868